# Experimental study on behaviors of low-Stokes number particles in weakly chaotic structures induced by thermocapillary effect within a closed system with a free surface

Takeru Oba, Aro Toyama, Takuma Hori, and Ichiro Ueno*
*Department of Mechanical Engineering, Faculty of Science and Technology, Tokyo University of Science, Chiba, Japan*

(Received 16 March 2019; published 15 October 2019)

We focus on the behaviors of the low-Stokes-number particles in a thermocapillary-induced convection within a closed geometry with a free surface, known as a half-zone liquid bridge. The motions of the spherical particles suspended by the bridge of a high-Prandtl-number liquid (Pr = 28.6) are tracked via two-dimensional and three-dimensional particle tracking velocimetry. Special attention is paid to the behaviors of the suspended particles in the flow regime in which coherent structures by the particles are realized; so-called particle accumulation structures (PASs). Through the experiments, we succeed in reconstructing three-dimensional trajectories of particles that form PASs, the toroidal core, and a structure wrapping the toroidal core. We illustrate the spatial and temporal correlations between the particles forming such three different coherent structures and corresponding regular flow structures; so-called Kolmogorov-Arnold-Moser (KAM) tori. It is found that the particles on the toroidal core exhibit helical motion through extracting the paths of the particles in azimuthal-axial planes with a small depth in the radial direction, which qualitatively corresponds to a Poincaré section.

DOI: 10.1103/PhysRevFluids.4.104002

## I. INTRODUCTION

Accumulation of suspended particles in a flow in open geometries has been investigated in nature and industrial applications after several pioneering works [1–3]. Such behaviors of suspended particles can be applied, for instance, to shape-based separation of rigid micro- or nanoscale particles in liquid phases [4–6]. In closed geometries, on the other hand, it has been found that such accumulations form unique coherent structures. Schwabe *et al.* [7] first indicated that the suspended particles in the thermocapillary-driven convection within a so-called half-zone (HZ) liquid bridge, which is one of the typical closed geometries with a free surface, spontaneously exhibit a coherent structure. The structure had a closed-loop shape, and rotated along the rotating flow induced by a so-called hydrothermal wave (HTW) [8] without changing its shape like a rigid body. Such a coherent structure, as shown in Fig. 1, was named a particle accumulation structure (PAS). After the milestone work by Schwabe *et al.* [7], occurring conditions as functions of the intensity of the thermocapillary-driven convection and the shapes of the liquid bridges have been investigated experimentally [9–11] and numerically [12–17].

Tanaka *et al.* [10] experimentally illustrated two major structures of the particle accumulations: the spiral-loop 1 (SL1) and spiral-loop 2 (SL2) PASs, depending on the winding number of the structures near the free surface. Such structures have been observed in different geometries, such as

*ich@rs.tus.ac.jp

 

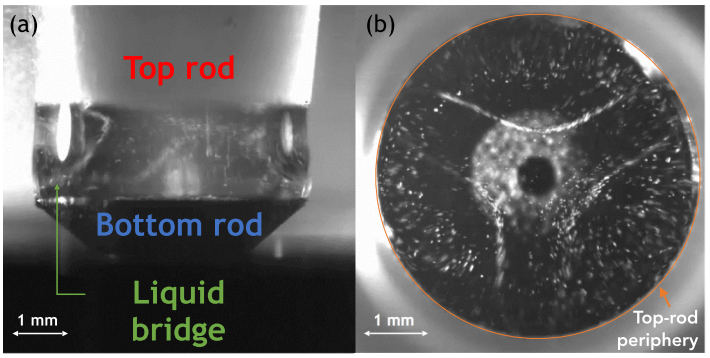


FIG. 1. Snapshots of liquid bridge with SL1 PAS as viewed from (a) side and (b) above through transparent top rod. A black hole at the center in panel (b) is the outlet of the tube for the liquid supply through the bottom rod. The white around the hole corresponds to the sediment; the particles settled on the surface of the bottom rod.

hanging droplets induced by the thermocapillary effect [18] and lid-driven cavities [19,20]. Within the geometries of the HZ liquid bridge, the particles reportedly form another structure called the "toroidal core" that emerges simultaneously with the PAS [10,21,22]; the core appears to form a toroidal structure, which is partially wrapped by the PAS.

Correlation between such coherent structures and the flow fields has been discussed by applying model-flow fields. Hofmann and Kuhlmann [12] first demonstrated the existence of regular flow regions known as Kolmogorov-Arnold-Moser (KAM) tori in a certain range of the flow intensity by using a traveling-wave-type model convection of a high-Prandtl-number fluid ($\mathrm{Pr} = 4$) in the HZ liquid bridge. The KAM tori are stationary and rigid under certain conditions in terms of Reynolds number Re in the rotating frame of reference; that is, the structures exhibit rigid-body-like rotating motion with the same angular velocity in the absolute coordinate system as the PAS [23,24]. They indicated that the topological convective fields resemble the coherent structures formed by the suspended particles, and that there exist several tori in addition to the chaotic region in the convective field. Then indirect comparison was made between the KAM tori in the model convection in the HZ liquid bridge and the coherent structures realized by spherical particles in the experiments [22,25]. By integrating images of the particles observed from above in the rotating frame of reference, it was first indicated that the suspended particles were attracted to form several coherent structures, which correspond to the KAM tori predicted. The flow fields exhibiting the coherent structures are thus realized below the threshold for the secondary instability in which the flow in the rotating frame of reference becomes time-dependent [26]. A series of numerical simulation on the motions of the spherical particles in the thermocapillary-driven flow were conducted by Romanò and Kuhlmann [17]. They successfully reproduced the coherent structures in the high-Pr liquid bridge applying the concept of a so-called "lubrication gap" near the free surface [12,23,27] in order to describe the particle motions in geometries with rigid or free boundaries [28] with the Maxey-Riley equation. Through the simulation, they indicated that the same accumulation is realized with and without taking account of inertia, even though the particles are heavier than the fluid. Note that Romanò and Kuhlmann [17] did not find a KAM torus corresponding to the core of particles, but found a core of particles that was transient in a long timescale in the cylindrical liquid bridge of $\mathrm{Pr} = 28$; the toroidal core becomes weakly chaotic in a high-Pr liquid bridge.

Experimental works using the particle tracking method have indicated that the coherent structures are formed by identical motions of the suspended spherical particles; three-dimensional behaviors of the particles forming the SL1- and SL2 PASs were investigated by applying particle tracking velocimetry (PTV) [29,30]. Nishimura *et al.* [21] tracked a particle forming the core as well as another one forming the PAS. Note that the particles were tracked for a period of $O(1\ \mathrm{s})$ in the

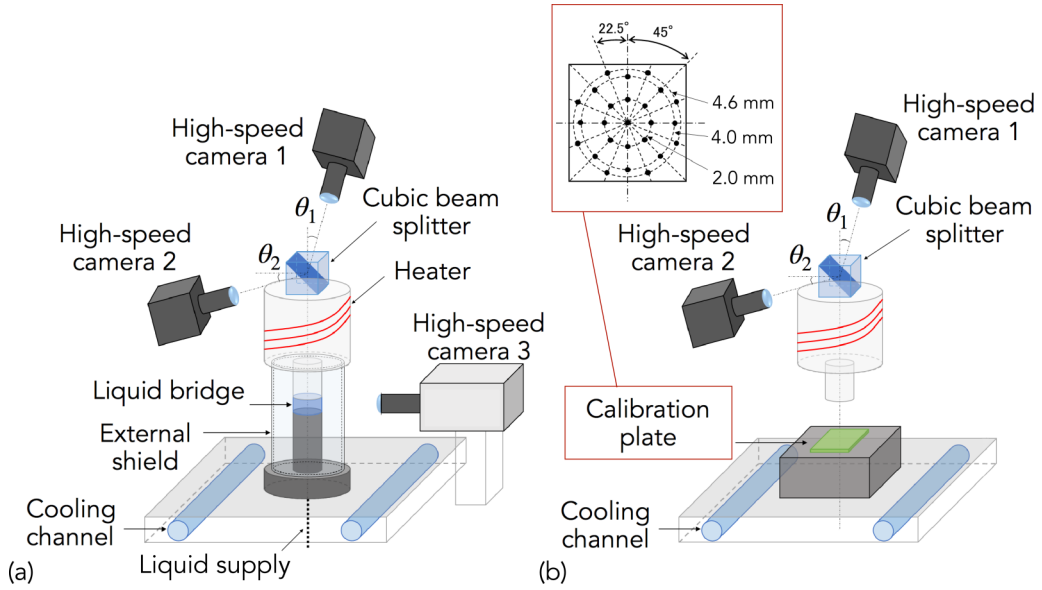


FIG. 2. Schematic diagram of experimental apparatus for 3-D PTV: (a) setup for particle tracking in liquid bridge, and (b) setup for camera calibration. Inset in frame (b) illustrates the dot pattern on the calibration plate.

previous studies. Yamaguchi *et al.* [31] conducted longer-period observation of the particle forming the core by applying a thin laser light sheet and indicated that the toroidal core is rather hard to observe, as indicated by Romanò and Kuhlmann [17], and that the particle would not be strongly attracted to the core but would migrate among coherent structures in the liquid bridge of such high Pr.

It is emphasized that spatial-temporal behaviors of a single particle attracted to form a coherent structure have not yet been widely discussed by considering correlations among particle behaviors, the coherent structures, and the topological convective structures of the KAM tori. In the present study, we conduct a series of experiments to capture those behaviors of spherical particles with two- and three-dimensional tracking methods in the rotating frame of reference. We pay special attention to its behaviors on the toroidal core, known as the weakly chaotic region within a high-Pr liquid bridge [17], as well as the SL1 PAS.

## II. EXPERIMENTS

The experimental apparatus with a three-dimensional particle tracking system is illustrated in Fig. 2. Figure 2(a) shows the apparatus for the particle tracking, and Fig. 2(b) shows the apparatus for the camera calibration. The apparatus for the particle tracking consists of two major parts: the liquid-bridge formation part, and the observation part. The details of the former are available in Toyama *et al.* [32], and details of the latter are almost the same as in Takakusagi and Ueno [18].

A liquid bridge forms between the coaxial cylindrical face-to-face rods as illustrated in Fig. 1. The parts for forming and sustaining the liquid bridge correspond to those described in Ref. [25]. The top rod is made of sapphire, which enables us to monitor the motion of the suspended particles through the transparent rod. The radius $R$ of the end surface to sustain the liquid is 2.5 mm. The top rod is heated to the designated temperature $T_h$ by a heater consisting of a nichrome wire wound around the rod. The temperature of the top rod is monitored by a K-type thermocouple embedded in the rod. The heater and the thermocouple are connected to the temperature controller (Model 335 Cryogenic Temperature Controller, Lake Shore Cryotronics, Inc., USA), and the temperature

of the rod is adjusted by proportional-integral-derivative (PID) control. The bottom rod is made of aluminum and its radius at the end surface is 2.5 mm, the same as $R$. The upper edge of the bottom rod is tapered at 45° and is coated with fluorine, for preventing undesignated liquid from dripping from the bottom rod. A small hole is drilled through the center of the bottom rod (seen as a black hole in the center of Fig. 1) and is connected to a syringe filled with the test fluid via a tube; the test liquid is supplied through the hole from the syringe controlled by the syringe pump. The temperature at the bottom rod is kept at $T_c = 20\,^{\circ}\mathrm{C}$ by using a cooling channel through its base block. We then realize a designated temperature difference $\Delta T = T_h - T_c$. The intensity of the thermocapillary effect is described by the Marangoni number $\mathrm{Ma} = |\gamma_T|\Delta T H/(\rho\nu\kappa)$, where $\gamma_T$ [N/(m K)] is the temperature coefficient of the surface tension $\gamma$, $\rho$ [kg/m$^3$] is the density, $\nu$ [m$^2$/s] is the kinematic viscosity, and $\kappa$ [m$^2$/s] is the thermal diffusivity of the test liquid. Through this research, the aspect ratio of the liquid bridge is fixed at $\Gamma = H/R = 0.68$, where $H$ is the height of the liquid bridge or the distance between the end surfaces to sustain the liquid. This condition firmly brings a stable formation of PAS with an azimuthal wave number $m = 3$ in traveling-wave-type convection with constant fundamental frequency [32].

The liquid bridge is concentrically surrounded by a glass shield of 25 mm in inner diameter and of 1.5 mm in thickness in order to fix the thermal boundary conditions around the liquid bridge as much as possible; this shield prevents undesignated buoyant flows of the ambient gas realized in the open system. A ZnSe window is installed at a tiny part in the azimuthal direction of the shield, which allows us to monitor the surface temperature via an infrared (IR) camera (Thermography R300, NEC Avio Infrared Technologies Co., Ltd., Japan) with a closeup lens (TVC-2100UB, NEC Avio Infrared Technologies Co., Ltd., Japan). We record the signal via the IR camera at a fixed frame rate of 60 fps with 320 × 240 pixels with a temperature resolution of 0.05 K at 30 °C. The sensor of this IR camera detects infrared light from 8 to 14 $\mu$m. Note that we do not have information on the absorption coefficient as the optical property of our own silicone oil, so we cannot conduct a precise evaluation of the temperature measured by the IR camera, as described in Ref. [18]. The data monitored by the IR camera do not indicate the actual temperature on the free surface but do indicate the qualitative variation of the surface temperature. In this article, we call this qualitative variation the "temperature" for the sake of brevity.

The shape of the liquid bridge is monitored through the shield to confirm its volume ratio $V/V_0$, where $V$ is the total volume of the liquid bridge itself, and $V_0$ is the volume between the end surfaces corresponding to $\pi R^2 H$. The volume ratio is kept constant as $V/V_0 \sim 1 \pm 0.1$ by supplying the test liquid through the hole via the syringe pump so as to prevent any changes in the volume ratio due to evaporation. Note that the supply of the test liquid is conducted at a minimum rate to avoid significant disturbances to the flow field by injection. The velocity of the injected liquid is less than $5.0 \times 10^{-3}$ $\mu$m/s, which is significantly smaller than that of the Marangoni convection; see, for instance, Niigaki and Ueno [30], who measured the velocity of the particle forming the SL2 PAS under $\mathrm{Ma} = 4.8 \times 10^4$ and $\Gamma = 0.64$ to find the absolute velocity $v_{ab}$ [mm/s] in the range $10 \lesssim v_{ab} \lesssim 50$ and the axial velocity $v_z$ [mm/s] in the range $-50 \lesssim v_z \lesssim 10$. The intensity of thermocapillary effect for the SL2 PAS is larger than the present case for the SL1 PAS, so one cannot make a direct comparison between these cases. Nevertheless, the order of the particle's velocity induced by the thermocapillary convection would be comparable.

The test liquid is 2-cSt silicone oil (KF96L-2cs, Shin-Etsu Chemical Co., Ltd., Japan), whose Prandtl number is of 28.6 at 25 °C. The physical properties of the test fluid $\rho$, $\nu$, $\kappa$, $\gamma$, and $\gamma_T$ are $8.73 \times 10^2$, $2.0 \times 10^{-6}$, $7.00 \times 10^{-8}$, $18.3 \times 10^{-3}$, and $-7 \times 10^{-5}$, respectively. These properties, except $\gamma_T$, are provided by the product company [33]. The temperature dependence of the kinematic viscosity is considered by using an empirical correlation [9,34] such as $\nu(T)/\nu_0 = \exp[5.892(25 - T)/(273.15 + T)]$, where $\nu_0$ is the kinematic viscosity of the test liquid at 25 °C, and $T$ is the temperature in degrees Celsius. The kinematic viscosity of the liquid bridge to determine the Marangoni number is evaluated as $\nu_{\mathrm{exp}}(T) = [\nu(T_h) + \nu(T_c)]/2$.

Gold-nickel-alloy–coated acrylic particles (Soken Chemical and Engineering Co. Ltd., Japan) are used as test particles, as per Gotoda *et al.* [35] and Toyama *et al.* [32]. The diameter and density

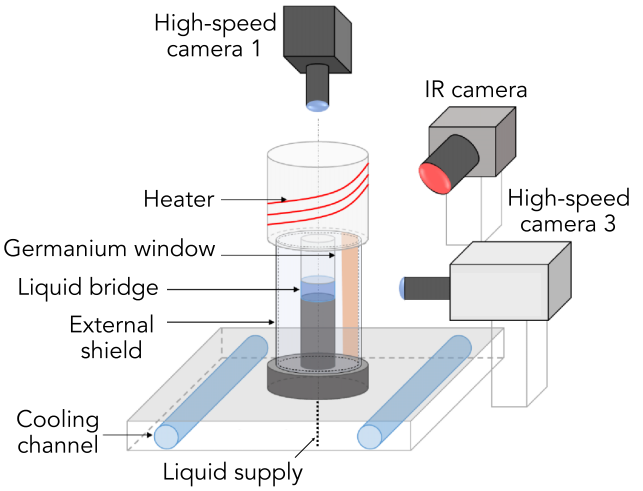


FIG. 3. Schematic diagram of apparatus for preliminary experiments to detect spatial and temporal correlation among flow field through top rod (via high-speed camera 1), thermal field over free surface (infrared camera), and dynamic deformation of free surface (high-speed camera 3).

of this particle are 30 $\mu$m and $1.49 \times 10^3$ kg/m$^3$, respectively. The Stokes number of the particles concerned is $3.0 \times 10^{-5}$ by using the definition $\mathrm{St} = \varrho d_\mathrm{p}^2/(18H^2)$ [12], where $\varrho$ is the density ratio between the particle $\rho_\mathrm{p}$ and the test fluid $\rho_\mathrm{f}$, and $d_\mathrm{p}$ is the particle diameter.

In this system, a cubic beam splitter is placed above the top rod [30], and the successive images of the particles suspended in the liquid bridge are captured by two synchronized high-speed complementary metal-oxide semiconductor (CMOS) cameras of 2048 × 2048 pixels at frame rates up to 500 frames per second (fps) (FASTCAM-Mini WX100, Photron, Inc., Japan). The incident angle of these cameras are tilted at $\theta_1$ and $\theta_2$ for high-speed camera 1 and 2, respectively. The triple-pattern-matching algorithm developed by Nishino *et al.* [36] is used for to track the particles. To realize particle tracking, we have to evaluate the so-called camera parameters by analyzing the given positions of the fine dots patterned on the calibration plate [see inset of Fig. 2(b)] [21]. This camera-calibration process is conducted before and after the experimental run.

To reconstruct the particle positions against the flow field induced by the HTW instability, it is indispensable to obtain the particle positions in the rotating frame of reference. In previous research [25,32,35], the phase correlation between PAS and the flow field was examined by monitoring the temperature variation over the free surface via an IR camera and the particle motion through the transparent top rod via a high-speed camera. In the present study, we use a trio of synchronized high-speed cameras, as shown in Fig. 2(a); we simultaneously observe the particle position with two high-speed cameras (high-speed camera 1 and 2 in the figure) from above and the dynamic surface deformation (DSD) via another high-speed camera (high-speed camera 3). Spatial correlations among the DSD, the PAS, and the surface temperature distribution were examined [25] with another experimental apparatus, as shown in Fig. 3. With this setup, we obtained the phase difference between the temperature variation over the free surface and the dynamic surface deformation of the liquid bridge (Fig. 4), because we focus on the traveling-wave-type flow field with a constant azimuthal phase velocity and we fix the azimuthal positions of the IR camera and the high-speed camera (high-speed camera 3), as conducted by Takakusagi and Ueno [18]. In addition, we use this setup for long-duration observations of the particles inside the liquid bridge in the radial-azimuthal plane as the two-dimensional tracking; the incident angle of the high-speed camera for the observation from above (high-speed camera 1) is zero; that is, the camera is aligned parallel to the $z$ axis of the liquid bridge.

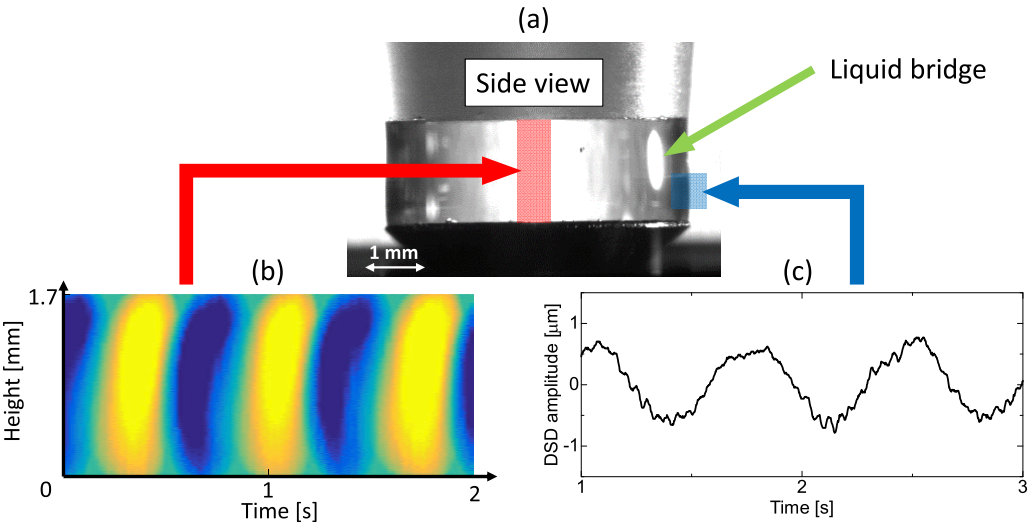


FIG. 4. Schematic of preliminary experiment: (a) side view of liquid bridge, (b) surface temperature deviation observed with infrared camera, and (c) dynamic surface deformation (DSD) of liquid bridge by high-speed camera 3 shown in Fig. 3.

## III. RESULTS AND DISCUSSION

### A. Two-dimensional analysis of particle motion

Figure 5 illustrates the map of typical coherent structures by the suspended particles inside the liquid bridge in the rotating frame of reference against the particle size and temperature difference. Figures 5(a)–5(d) show the results with $d_p = 5$, 10, 15, and 30 $\mu$m, respectively. Each image is obtained by accumulating 625 inverted frames (or for 1.25 s) in the rotating frame of reference under each condition. In this figure, the direction of HTW in the laboratory frame is counterclockwise for all images. Depending on the particle sizes, the occurring conditions of particle accumulations become different. The results indicate that the particles travel inside the liquid bridge except in the center region to form a particle-depletion zone with a triangle shape. Some of the particles gather to exhibit dense line-like structures [see, for instance, Figs. 5(a) and 5(b)]. As $\Delta T$ or the corresponding Ma increases, more and more particles gather on this structure (black in frames). The majority of the particles have aggregated to realize almost perfect accumulation at $\Delta T = 40$ K. As seen in the column of $\Delta T = 44$ K, the line-like structure becomes vague; the particles move away from the coherent structure to chaotic regions. Although there exist morphological differences by changing the particle diameter, the scenarios of the spatial distributions of the particles trajectories are qualitatively the same. When one pays attention to the condition under $\Delta T = 40$ K, the line-like structure becomes denser as the particle size increases. It is found that the larger particles tend to be attracted to the core, which is one of the other coherent structures [10]. More detailed variations of the coherent structures by varying $\Delta T$ or the corresponding Ma are described by Gotoda *et al.* [25]. The SL2 PAS emerges under larger $\Delta T$ or Ma [see, for instance, Fig. 5(a) at $\Delta T = 48$ K] than that for the SL1 PAS [see, for instance, Fig. 5(a) at $\Delta T = 40$ K], as indicated in previous studies [10,32]. It is also illustrated that it becomes rather difficult for the particles to form the SL2 PAS with larger particles [as shown in row (d) of Fig. 5]. In the present study, we focus on the flow field with $d_p = 30$ $\mu$m under $\Delta T = 40$ K (as surrounded by the rectangular frame) in the following: the particles demonstrate PAS [Fig. 5(A)], the core [Fig. 5(B)], and a winding structure wrapping the core [Fig. 5(C)], as illustrated in the enlarged view under this condition. Those coherent structures have spatial characteristics similar to those of KAM tori; $T_3^3$ [Fig. 5(A)], $T_{core}$ [Fig. 5(B)], and $T_3^9$ [Fig. 5(C)] as first indicated by Kuhlmann *et al.* [22].

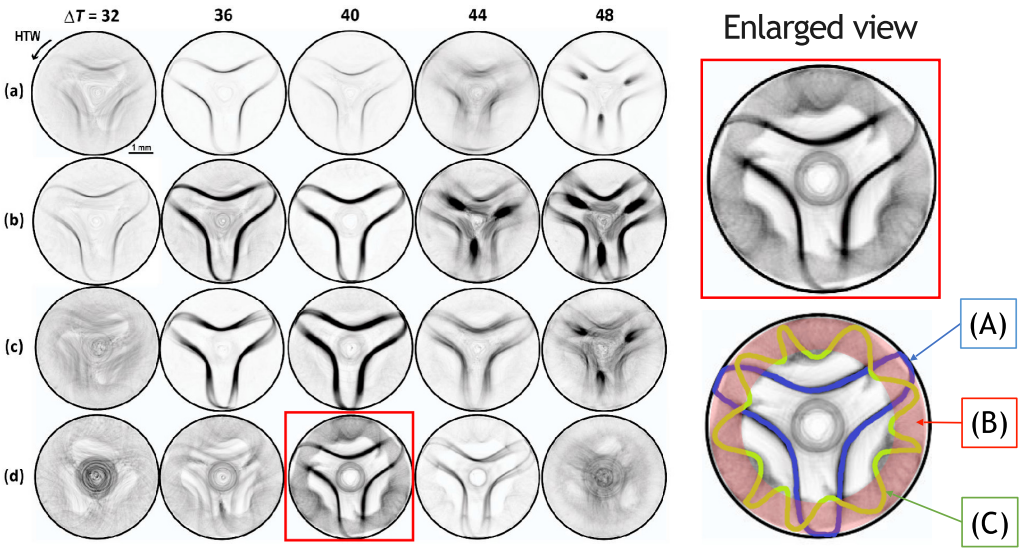


FIG. 5. (left) Map of coherent structures by suspended particles in rotating frame of reference against particle size $d_p$ and temperature difference $\Delta T$. Black dots correspond to the particles and white area corresponds to the region where no particles exist. The direction of HTW in the laboratory frame is counterclockwise for all images. Rows (a)–(d) indicate the results with $d_p = 5$, 10, 15, and 30 $\mu$m, respectively. Each image is obtained by accumulating 625 inverted frames in the rotating frame of reference under each condition. (right) Enlarged view of pattern under target condition in this study with (d) $d_p = 30$ $\mu$m under $\Delta T = 40$ K. The particles demonstrate the coherent structures of (A) PAS, (B) the core, and (C) a winding structure wrapping the core. Corresponding Kolmogorov-Arnold-Moser (KAM) tori are indicated by (A) $T_3^3$, (B) $T_{core}$, and (C) $T_3^9$.

We first focus on long-duration observations of the particles on the PAS and the core with a two-dimensional observation system (as shown in Fig. 3). The left frames of Fig. 6(a) and 6(b) illustrate typical examples of temporal variations of the radial positions of the particle on the PAS and the core, respectively. Their power spectrum densities by the fast Fourier transform (FFT) are illustrated in the right frames. The particle on the PAS, or the particle attracted to $T_3^3$ hereafter, exhibits a regular motion with a fundamental frequency of 2.5 Hz. This frequency corresponds to that of the basic turnover motion of the particle. Note that the fundamental frequency of the HTW is 1.35 Hz under this condition. The particle travels close to the free surface described as $r = r_{max}^{(PAS)}$, and then returns to the interior region up to $r = r_{min}^{(PAS)}$. Note that the value $r_{max}^{(PAS)}$ exceeds 2.5 mm, which corresponds to the radius $R$. The radius $R$ does not correspond to the radial position of the free surface, but to the radius of the end surfaces to sustain the liquid bridge. This situation ($r_{max}^{(PAS)}/R > 1$) reflects the deformation of the liquid bridge [28]; the liquid bridge exhibits a deformation inward in the top half and outward in the bottom half in the $r$ direction due to the gravity effect. The particle attracted $T_3^3$ approaches very close to the free surface. Note that there exist the DSD in addition to the static deformation of the liquid bridge. The amplitudes of the DSD and the static deformation are of $O(1\ \mu m)$ and $O(100\ \mu m)$, respectively, thus the value of $r_{max}^{(PAS)}$ depends on the deformation by the gravity effect. On the other hand, the particle on the core, or the particle attracted to $T_{core}$ hereafter, travels inside the liquid bridge with higher frequencies in a range from 4.4 to 5.2 Hz. Because of the correlations as $r_{max}^{(PAS)} > r_{max}^{(core)}$ and $r_{min}^{(PAS)} < r_{min}^{(core)}$, the turnover frequency of the particle attracted to $T_{core}$ becomes much higher. There exist multiple peaks in frequency at around 4.4 Hz, and it is impossible to define a single fundamental frequency for the motion of the particle attracted to $T_{core}$. This result clearly reflects the prediction that the core becomes rather chaotic for high Pr [17]. In

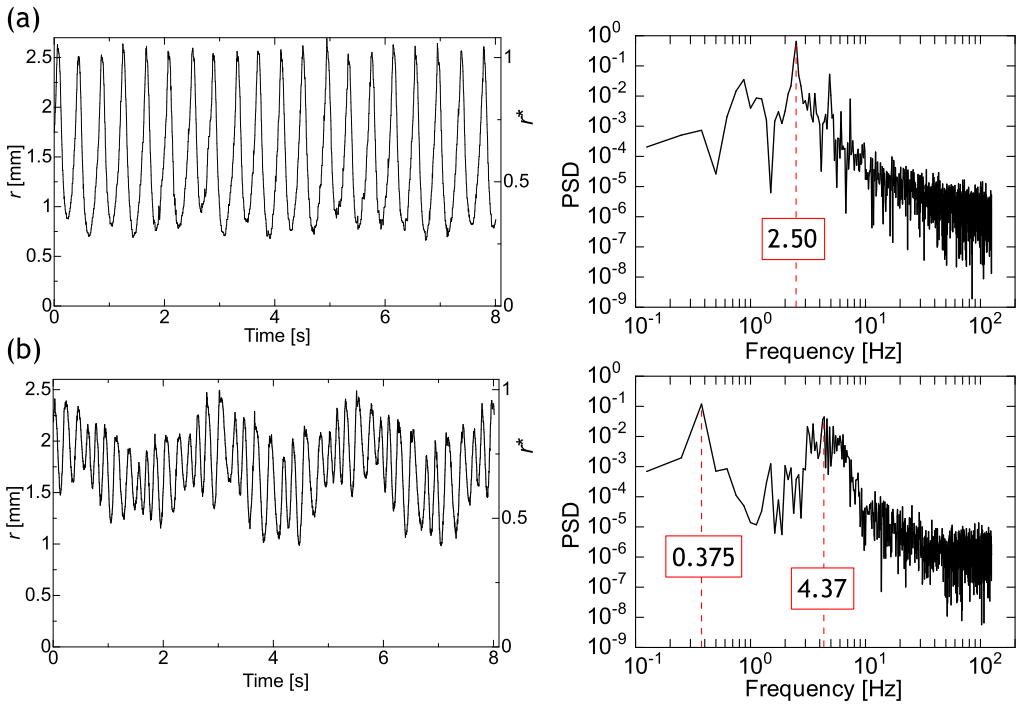


FIG. 6. Typical examples of (left) temporal variations of radial positions of particle on (a) PAS and (b) core and (right) their power spectrum densities obtained via two-dimensional particle tracking.

addition to the basic turnover motion, one finds modulation in the particle motion with a frequency at around 0.4 Hz. Such modulation results in a wider existence region in $r$ for the core when one obtains projected images by accumulating successive data, as shown in Fig. 5.

Figure 7 indicates spatial variations in particle position $r$ against azimuthal position $\theta$ in the laboratory frame; Fig. 7(a) shows the particle attracted to $T_3^3$ and Fig. 7(b) shows that attracted to $T_{core}$. The data shown here are the same as those shown in Fig. 6. The particle attracted to $T_3^3$ exhibits regular motion with almost periodic behavior, as seen in the temporal variation [Fig. 6(a)]. The interval of $\theta$ between each maximum position $r = r_{max}^{(PAS)}$ is almost constant. Thus, the net phase velocity in the azimuthal direction is constant for the particle to form the PAS [29]. The particle attracted to $T_{core}$, on the contrary, exhibits back-and-forth behaviors in a limited range of $\theta$ (e.g., at $\theta \sim 1020$ and $\sim 1180$ in the zoomed view) in addition to the basic turnover motions. Such back-and-forth motions for the particles forming the core were also observed in previous studies [10,21].

We now focus on the spatial correlation between the particles attracted to $T_{core}$ and the PAS itself. Figure 8 illustrates the spatial variations of the particle in the rotating frame of reference, which coincides that of the PAS. Figure 8(a) shows a snapshot of PAS observed from above. The azimuthal position $\phi$ is defined as follows: we detect the position at which the particle approaches closest to the free surface, $r_{max}^{(PAS)}$. We then evaluate the mean position in $\theta$ at $r = r_{max}^{(PAS)}$ for all particles detected on PAS as $\theta_0 = \Sigma_{i=1}^{N} \theta_{r=r_{max}^{(PAS)}}/N$ by considering threefold symmetry. This position is defined as $\phi = 0$; thus, $\phi = \theta - \theta_0$. Hereinafter, we call this position the tip of the PAS blade. In the frame, we put a red circle to indicate the particle concerned; that is, the particle attracted to $T_{core}$. In Fig. 8(b), we plot the radial positions of the particle against $\phi$. Note that the data plot in this frame are the same as shown in Figs. 6(b) and 7(b). Another note is that we conduct successive tracking of a single particle on the core, thus the particle exhibits multiple rotations against the

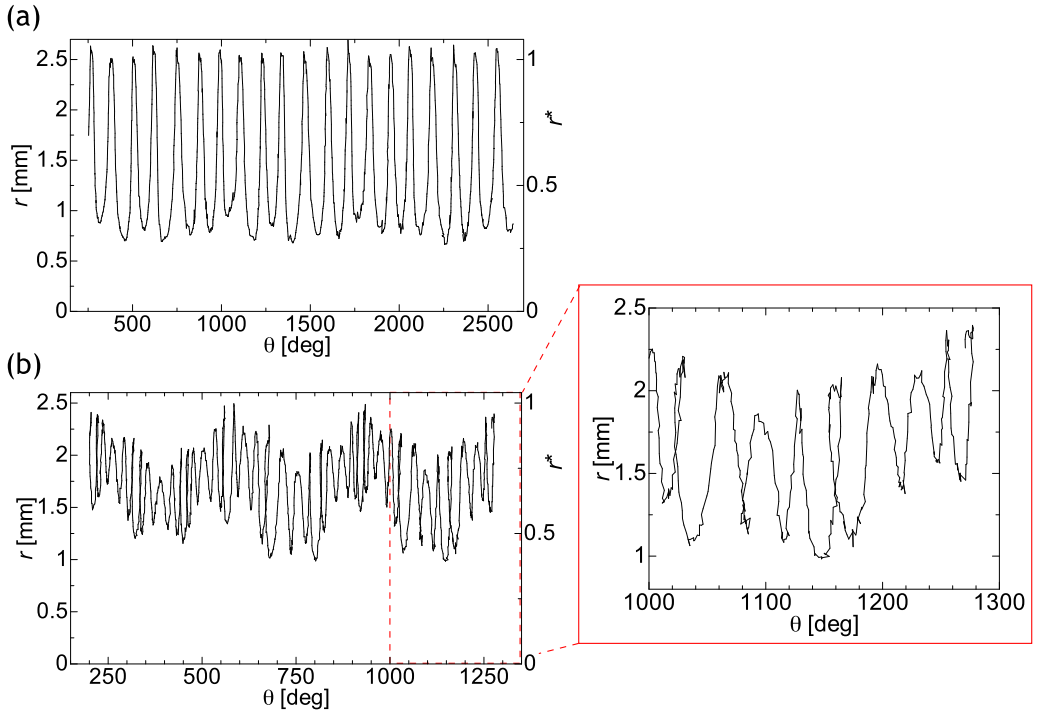


FIG. 7. Spatial variations of position in $r$ against azimuthal position $\theta$ in the laboratory frame of a single particle attracted to (a) $T_3^3$ and (b) $T_{core}$.

PAS whose location is fixed in the rotating frame of reference. To express the multiple rotations, we describe the azimuthal position $\phi'$ starting from the tip of the PAS with the number of rotation $n$; $\phi' = \phi + 2\pi n$. Red lines indicate the positions of the tip of the PAS blades, $2\pi(k-1)/3$, with integer $k$. It is found that the back-and-forth motions emerge between the tips of the PAS blades. One cannot predict, however, precise locations where such motion is exhibited between the tips. This is a significant sign that the core becomes rather chaotic, as predicted [17]. Tanaka *et al.* [10] found that the toroidal core has a shape with larger width between the tips of the PAS blades, and

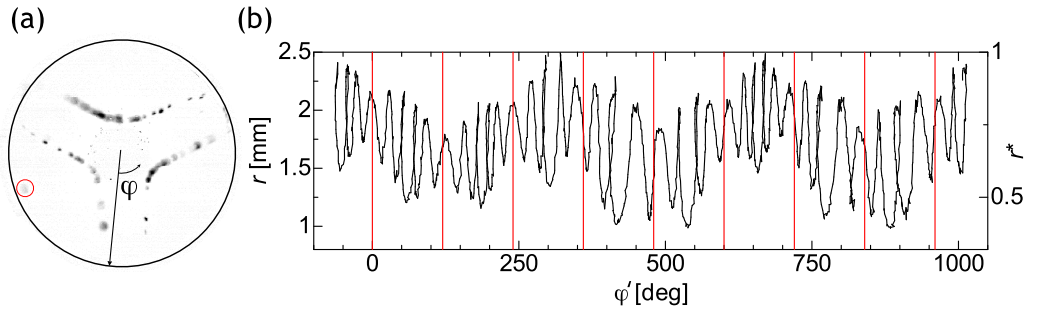


FIG. 8. (a) Snapshot of PAS observed from above. Azimuthal position $\phi$ is defined as the angle from the tip of the PAS blades. The particle in the red circle corresponds to the particle attracted to $T_{core}$. (b) Radial positions of particle attracted to $T_{core}$ against $\phi$. To express the multiple rotation, the azimuthal position $\phi'$ starting from the tip of PAS with the number of rotation $n$; $\phi' = \phi + 2\pi n$. Red lines indicate the positions of the tip of the PAS blades, $2\pi(k-1)/3$ with integer $k$.

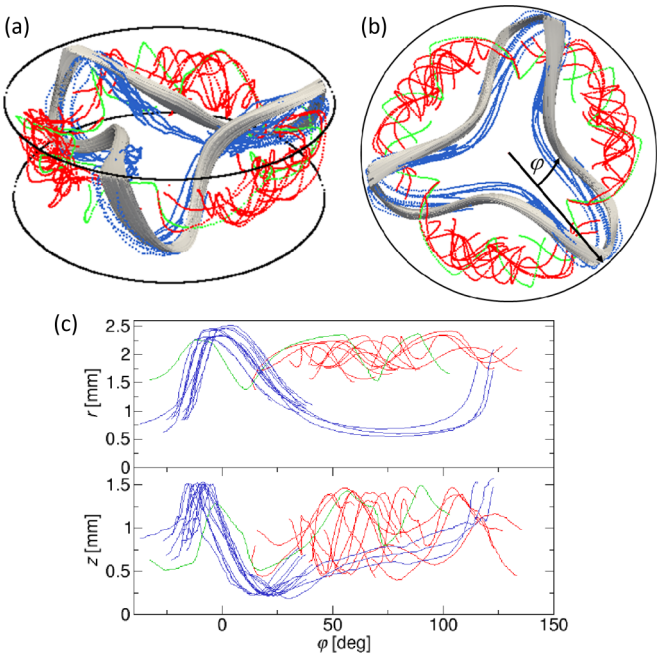


FIG. 9. Reconstructed trajectories of the particles in (a) bird's-eye and (b) top views. The figures consist of the trajectories of the particles on PAS (14 trajectories in blue), on the core (16 trajectories in red) and on the structure wrapping the core (3 trajectories in green). The direction of HTW is clockwise, and the net direction of the particles on PAS is counterclockwise (in the positive $\phi$ direction) in the laboratory frame. Bundles of path lines to form PAS obtained by the numerical simulation [37] are also drawn in gray. (c) Distributions of all trajectories in $r$-$\phi$ (top) and $z$-$\phi$ (bottom) planes.

a smaller width near the blades. The present result agrees with their result; $\Delta r_{\mathrm{core}} = r_{\mathrm{max}}^{(\mathrm{core})} - r_{\mathrm{min}}^{(\mathrm{core})}$ between the blades is larger than that near the tips of the PAS blades indicated by red lines. As mentioned above, modulative motions of the particles attracted to $\mathrm{T}_{\mathrm{core}}$ result in such a shape of the toroidal core in the projected view.

### B. Three-dimensional analysis of particle motion

In the following, we focus on three-dimensional correlation among the particles forming different coherent structures. Because of the limitation of the common field of view of two synchronized cameras tilted against the liquid-bridge center line, we cannot avoid periods when we cannot track the same particles by two cameras simultaneously. This means that we have some periods during which we cannot detect the particle images. Thus the observation period for three-dimensional reconstruction becomes rather shorter than those for two-dimensional tracking experiments.

Figures 9(a) and 9(b) illustrate the reconstructed trajectories of the particles in the bird's-eye and top views, respectively. The figures consist of the trajectories of the particles on the PAS (14 trajectories in blue), on the core (16 trajectories in red), and on the structure wrapping the core (3 trajectories in green). We obtain the trajectories in one-third of the region of the liquid bridge in the azimuthal direction by the experiments. Because of the threefold rotational symmetric structure of the flow field, we plot the same results repeatedly with a phase difference of $\pm 2\pi/3$ in the rest region. Bundles of path lines to form PAS obtained by the numerical simulation [37] are also drawn in gray. Figure 9(c) shows the distributions of all trajectories in the $r$-$\phi$ (top) and $z$-$\phi$ (bottom) planes. The trajectories of the particles attracted to $\mathrm{T}_3^3$ are distributed regularly in $\phi$ in the ranges

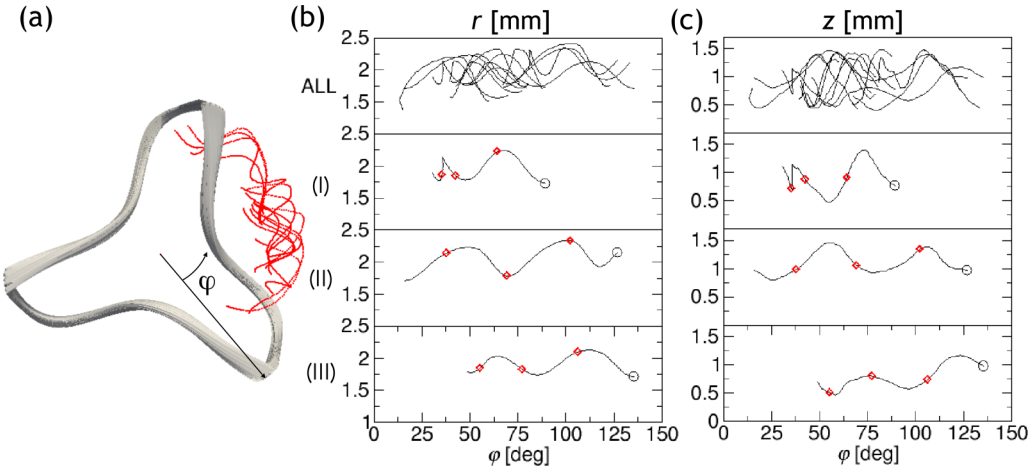


FIG. 10. (a) Top view of trajectories of particles attracted to core. Path lines by numerical result [37] are also drawn. Three examples of trajectories in (b) $r$ and (c) $z$ positions against $\phi$. The black circle indicates the starting point of each tracked data, and the red diamond is plotted every 50 frames.

$0.5\ \text{mm} \lesssim r \lesssim 2.5\ \text{mm}$ and $0.25\ \text{mm} \lesssim z \lesssim 1.6\ \text{mm}$. As the particles approach the free surface ($-20^\circ \lesssim \phi \lesssim 0^\circ$), they rise in the liquid bridge toward the top-end surface. After coming closest to the free surface, they slide down toward the bottom-end surface and sneak into the interior region of the liquid bridge ($0^\circ \lesssim \phi \lesssim 25^\circ$). They travel to the deepest in $r$ ($r = r_{\text{min}}^{(\text{PAS})}$) as gradually ascending for a while ($25^\circ \lesssim \phi \lesssim 100^\circ$), then change their direction of motion steeply toward the free surface again ($100^\circ \lesssim \phi \lesssim 120^\circ$). The particles on the core (in red), on the other hand, distribute in narrower area, especially in $r$. Their motion in the $\phi$ direction seems rather random, as observed in Tanaka *et al.* [10]. Detailed observation will be made via Fig. 10. The particle on the structure wrapping the core, or the particle attracted hereafter to $\text{T}_3^9$, distributes almost over the same region where the particles are attracted to $\text{T}_{\text{core}}$. The variation in the $\phi$ direction in a turnover cycle is larger than that for the particle attracted to $\text{T}_{\text{core}}$, and smaller than that for the particle attracted to $\text{T}_3^3$. The particle attracted to $\text{T}_3^9$ and to $\text{T}_3^3$ never exhibits back-and-forth motion by that attracted to $\text{T}_{\text{core}}$.

Figure 10(a) illustrates the trajectories of the particles attracted to $\text{T}_{\text{core}}$. To indicate the spatial correlation with the PAS, path lines by the numerical result [37] are again drawn. We then pick up three trajectories among the results, and illustrate their $r$ [Fig. 10(b)] and $z$ [Fig. 10(c)] positions against $\phi$. The black circle indicates the starting point of each tracked data, and red diamonds are plotted every 50 frames. We find that these particles in the core travel in the negative $\phi$ direction. This net direction is the same as HTW, but opposite to the particles on PAS [10,21]. It is indicated that the trajectories consist of two major regimes: one is rather periodic as seen in particles (II) and (III), and the other is a regime with a sharp change of the direction of the motion as seen at $\phi \sim 40^\circ$ for particle (I). Such sharp changes of the motion corresponding to the back-and-forth motion observed in the two-dimensional tracking are never observed for the particles attracted to $\text{T}_3^3$.

To illustrate spatial distributions of the trajectories of the particles attracted to various regular flow structures, the paths in $z$-$\phi$ space within $\Delta r$ at different $r$ in the outer half of the liquid bridge are extracted, as shown in Fig. 11. Although this space has finite depth in the $r$ direction, such an illustration may uncover information similar to the Poincaré section [38]. All data shown here are the same as in Figs. 9 and 10; the propagation direction of HTW is in the negative $\phi$ direction in the laboratory frame. This figure consists of the paths in Fig. 11(a) for $r/R \geqslant 0.9$, or near the free surface, and in the narrow region of $\Delta r = 0.25$ mm or $\Delta(r/R) = 0.1$ in depth $0.8 \leqslant r/R < 0.9$ [Fig. 11(b)], $0.7 \leqslant r/R < 0.8$ [Fig. 11(c)], and $0.6 \leqslant r/R < 0.7$ [Fig. 11(d)]. The particles attracted

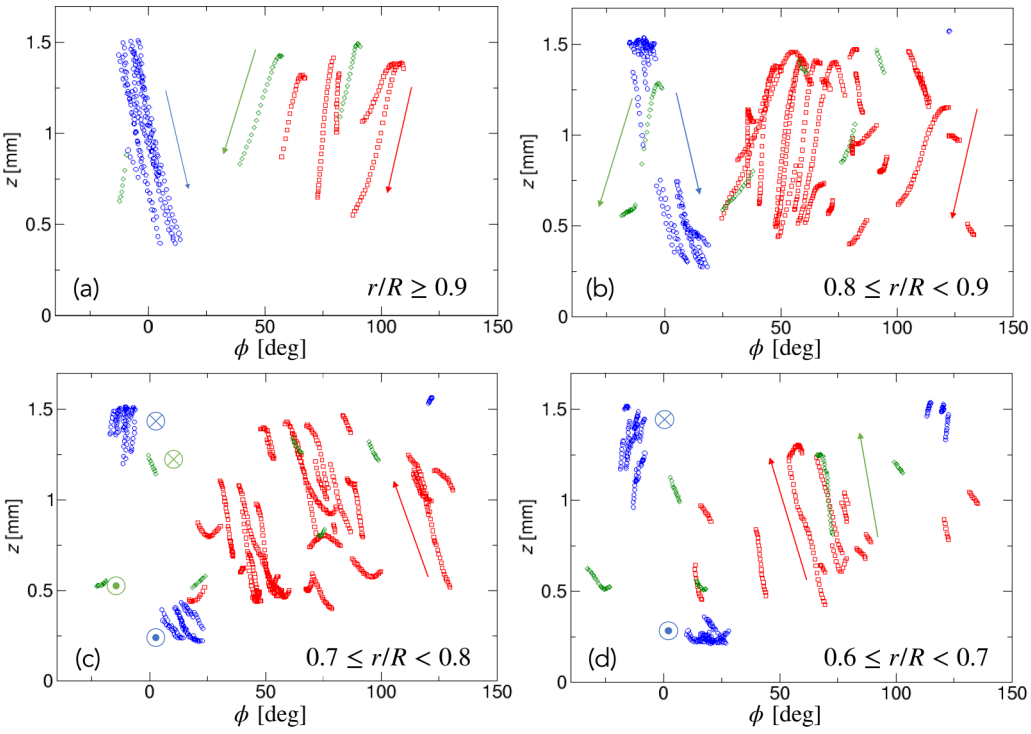


FIG. 11. Spatial distributions of paths in $z$-$\phi$ space in (a) $r/R \geqslant 0.9$, (b) $0.8 \leqslant r/R < 0.9$, (c) $0.7 \leqslant r/R < 0.8$, and (d) $0.6 \leqslant r/R < 0.7$. The particles attracted to $T_3^3$, $T_{core}$, and $T_3^9$ are drawn in blue, red, and green, respectively. Arrows in each frame indicate the direction of motions of the particles concerned. The direction in $r$ of the particle motion is also indicated in panels (c) and (d). The symbol $\odot$ indicates motion toward the free surface (or in the positive $r$ direction), and $\otimes$ indicates motion toward the center axis of the liquid bridge (or in negative $r$ direction).

to $T_3^3$, $T_{core}$, and $T_3^9$ are drawn in blue, red, and green, respectively. Arrows in each frame indicate the direction of particle motions. The direction in $r$ of the particle motion is also indicated in Figs. 11(c) and 11(d); the symbol $\odot$ indicates motion toward the free surface (or in the positive $r$ direction), and the symbol $\otimes$ indicates motion toward the center axis of the liquid bridge (or in the negative $r$ direction). Note again that $R$ is the radius of the end surfaces of the rods to sustain the liquid bridge, not the position of the free surface in the $r$ direction at each $z$. Since we do not have the free-surface positions $r = r_{FS}(t, \phi, z)$, the distances between the free surface and the particles are not detectable in the present experiments.

In the region of Fig. 11(a) near the free surface, the particles attracted to $T_3^3$ travel downward successively with almost constant angle of propagation. It is emphasized again that we detect particle paths within a thin tubular region with a finite thickness $\Delta r$. This is why successive paths appear. Note that the azimuthal direction of the net motions of those particles is in positive $\phi$, which is opposite that of HTW. Such features were pointed out in previous research as well [10,11,29,32]. The particles attracted to $T_{core}$ and $T_3^9$, on the other hand, travel downward in the negative $\phi$ direction. As seen in Fig. 9 as well as in the prediction by Mukin and Kuhlmann [24], we have the same correlation as $r_{max}^{(PAS)} > r_{max}^{(core)}$, so that fewer paths exist in this region than the particles attracted to $T_3^3$. Slightly shifted to the interior region, $0.8 \leqslant r/R < 0.9$ [Fig. 11(b)], the paths of the particles attracted to $T_3^3$ are located separately near the top-end surface ($z \sim 1.5$ mm) and the bottom-end surface ($z \sim 0.5$ mm). Such a distribution clearly reflects the winding tubular structure of $T_3^3$. The particles attracted to $T_{core}$ and $T_3^9$ travel downward slightly inclined against $z$ in the negative $\phi$

direction, as seen in Fig. 11(a) near the free surface. One finds split distributions of the paths of the particles attracted to $T_3^9$, as seen for those attracted to $T_3^3$. As for the particles attracted to $T_{core}$, one finds two types of the paths: one with successive plots, and the other with split plots. This is because $T_3^3$ and $T_3^9$ have winding structures with a finer width, and $T_{core}$ has toroidal structure with larger width, which was also indicated by Kuhlmann *et al.* [22]. Focusing on the particles attracted to $T_{core}$, we consider that the particles with the successive and split paths locate in inner and outer regions, respectively, of the toroidal structure intersected with an annular tube $\Delta r$ in depth. When one looks in the deeper region, $0.7 \leqslant r/R < 0.8$ [Fig. 11(c)] and $0.6 \leqslant r/R < 0.7$ [Fig. 11(d)], it becomes significant that the paths of the particles attracted to $T_3^3$ and $T_3^9$ are split into two. The particles travel outward in $r$ near the top-end surface, and inward in $r$ near the bottom-end surface. When one pays attention to the particles attracted to $T_{core}$, one finds significant change of the behaviors. Those particles travel upward with a slightly inclined angle against the $z$ axis in the negative $\phi$ direction. One also finds that there exist not only successive paths like those attracted to $T_3^3$ and $T_3^9$ as seen in Fig. 11(a), but also separated groups of the paths in the upper and bottom halves, especially in Fig. 11(c). This region corresponds to the inner half region of the core in the $r$ direction. According to such distributions of the paths with different inclined angles in this region and in the outer half region seen in Fig. 11(b), $0.8 \leqslant r/R < 0.9$, we find that the particles attracted to $T_{core}$ exhibit helical motions in the tori in the rotating frame of reference. We also find that the particles travel not only on the surface, but also in the interior of $T_{core}$. For the latter, such a feature corresponds to the prediction by Muldoon and Kuhlmann [14] for the modeled flow field with $Pr = 4$ fluids. The spatial resolution in the experiments is far beyond that in the numerical simulation, but it must be emphasized that this is the first capture of the three-dimensional behaviors of particles attracted to $T_{core}$.

## IV. CONCLUDING REMARKS

We experimentally investigate the behaviors of low-Stokes-number particles in a thermocapillary-induced convection within a closed geometry with a free surface, known as the half-zone liquid bridge. Special attention is paid to the behaviors of the suspended spherical particles in the traveling-wave-type flow regime in which coherent structures by the particles are realized; the so-called particle accumulation structures (PASs). Temporal variation of the position of the particles suspended to the bridge of the high-Prandtl-number liquid ($Pr = 28.6$) are detected via a two-dimensional particle tracking method for a longer period and a three-dimensional method.

We successfully illustrate the spatial and temporal correlations among the particles consisting of three coherent structures; the PAS, the toroidal core, and a structure wrapping the toroidal core in the reference frame rotating azimuthally with the flow induced by the hydrothermal wave instability. Correlations between the coherent structures and so-called Kolmogorov-Arnold-Moser (KAM) tori corresponding to $T_3^3$, $T_{core}$, and $T_3^9$ realized in the convection are discussed. It is indicated that the path lines of the particles forming PAS exist in a certain range, especially near the free surface, to form a thin bundle-like structure. The particles forming the PAS, or the particles attracted to $T_3^3$, exhibit identical motions even in the azimuthal direction in addition to the turnover behaviors. On the other hand, the particles forming the toroidal core, or the particles attracted to $T_{core}$, show rather complex behaviors. They follow basic turnover motion in the $r$-$z$ plain, but move randomly in the azimuthal direction, as predicted by Romanò and Kuhlmann [17]. Through the three-dimensional monitoring of the paths of the trajectories of the particles in $z$-$\phi$ space within $\Delta r$ at different $r$, we find that the particles attracted to $T_{core}$ exhibit helical motions in the tori in the rotating frame of reference, and that the particles travel not only on the surface, but also in the interior of $T_{core}$.

## ACKNOWLEDGMENTS

We acknowledge Professor Koichi Nishino, Dr. Taishi Yano (Yokohama National University, Japan), and Professor Masahiro Motosuke (Tokyo University of Science) for invaluable support to carry out a series of experiments with three-dimensional particle tracking velocimetry. We

also gratefully acknowledge Professor Dr. Hendrik C. Kuhlmann and Dr. Francesco Romanò (TU Wien, Austria) for fruitful discussions. This study was financially supported by Grant-in-Aid for Challenging Exploratory Research (Project No. 16K14176) from the Japan Society for the Promotion of Science (JSPS).

[1] G. Segré and A. Silberberg, Radial particle displacements in poiseuille flow of suspensions, Nature (London) **189**, 209 (1961).
[2] G. Segré and A. Silberberg, Behaviour of macroscopic rigid spheres in poiseuille flow part 1. Determination of local concentration by statistical analysis of particle passages through crossed light beams, J. Fluid Mech. **14**, 115 (1962).
[3] G. Segré and A. Silberberg, Behaviour of macroscopic rigid spheres in poiseuille flow part 2. Experimental results and interpretation, J. Fluid Mech. **14**, 136 (1962).
[4] B. Behdani, S. Monjezi, M. J. Carey, C. G. Weldon, J. Zhang, C. Wang, and J. Park, Shape-based separation of micro-/nanoparticles in liquid phases, Biomicrofluidics **12**, 051503 (2018).
[5] H. Haddadi, H. Naghsh-Nilchi, and D. Di Carlo, Separation of cancer cells using vortical microfluidic flows, Biomicrofluidics **12**, 014112 (2018).
[6] J. L. Colón Quintana, T. Heckner, A. Chrupala, J. Pollock, S. Goris, and T. Osswald, Experimental study of particle migration in polymer processing, Polym. Compos. **40**, 2165 (2018).
[7] D. Schwabe, P. Hintz, and S. Frank, New features of thermocapillary convection in floating zones revealed by tracer particle accumulation structure (PAS), Microgravity Sci. Technol. **9**, 163 (1996).
[8] M. K. Smith and S. H. Davis, Instabilities of dynamic thermocapillary liquid layers. Part 1. Convective instabilities, J. Fluid Mech. **132**, 119 (1983).
[9] I. Ueno, S. Tanaka, and H. Kawamura, Oscillatory and chaotic thermocapillary convection in a half-zone liquid bridge, Phys. Fluids **15**, 408 (2003).
[10] S. Tanaka, H. Kawamura, I. Ueno, and D. Schwabe, Flow structure and dynamic particle accumulation in thermocapillary convection in a liquid bridge, Phys. Fluids **18**, 067103 (2006).
[11] D. Schwabe, A. I. Mizev, M. Udhayasankar, and S. Tanaka, Formation of dynamic particle accumulation structures in oscillatory thermocapillary flow in liquid bridges, Phys. Fluids **19**, 072102 (2007).
[12] E. Hofmann and H. C. Kuhlmann, Particle accumulation on periodic orbits by repeated free surface collisions, Phys. Fluids **23**, 072106 (2011).
[13] D. E. Melnikov, D. O. Pushkin, and V. M. Shevtsova, Accumulation of particles in time-dependent thermocapillary flow in a liquid bridge: Modeling and experiments, Eur. Phys. J. Spec. Top. **192**, 29 (2011).
[14] F. H. Muldoon and H. C. Kuhlmann, Coherent particulate structures by boundary interaction of small particles in confined periodic flows, Phys. D **253**, 40 (2013).
[15] M. Lappa, Assessment of the role of axial vorticity in the formation of particle accumulation structures in supercritical Marangoni and hybrid thermocapillary-rotation-driven flows, Phys. Fluids **25**, 012101 (2013).
[16] F. H. Muldoon and H. C. Kuhlmann, Different particle-accumulation structures arising from particle-boundary interactions in a liquid bridge, Int. J. Multiphase Flow **59**, 145 (2014).
[17] F. Romanò and H. C. Kuhlmann, Finite-size Lagrangian coherent structures in thermocapillary liquid bridges, Phys. Rev. Fluids **3**, 094302 (2018).
[18] T. Takakusagi and I. Ueno, Flow patterns induced by thermocapillary effect and resultant structures of suspended particles in a hanging droplet, Langmuir **33**, 13197 (2017).
[19] F. Romanò, S. Albensoeder, and H. C. Kuhlmann, Topology of three-dimensional steady cellular flow in a two-sided anti-parallel lid-driven cavity, J. Fluid Mech. **826**, 302 (2017).
[20] F. Romanò, H. Wu, and H. C. Kuhlmann, A generic mechanism for finite-size coherent particle structures, Int. J. Multiphase Flow **111**, 42 (2019).

[21] M. Nishimura, I. Ueno, K. Nishino, and H. Kawamura, 3D PTV measurement of oscillatory thermocapillary convection in half-zone liquid bridge, Exp. Fluids **38**, 285 (2005).
[22] H. C. Kuhlmann, R. V. Mukin, T. Sano, and I. Ueno, Structure and dynamics of particle-accumulation in thermocapillary liquid bridges, Fluid Dyn. Res. **46**, 041421 (2014).
[23] H. C. Kuhlmann and F. H. Muldoon, Particle-accumulation structures in periodic free-surface flows: Inertia versus surface collisions, Phys. Rev. E **85**, 046310 (2012).
[24] R. V. Mukin and H. C. Kuhlmann, Topology of hydrothermal waves in liquid bridges and dissipative structures of transported particles, Phys. Rev. E **88**, 053016 (2013).
[25] M. Gotoda, A. Toyama, M. Ishimura, T. Sano, M. Suzuki, T. Kaneko, and I. Ueno, Experimental study of coherent structures of finite-size particles in thermocapillary liquid bridges, Phys. Rev. Fluids **4**, 094301 (2019).
[26] T. Ogasawara, K. Motegi, T. Hori, and I. Ueno, Secondary instability induced by thermocapillary effect in half-zone liquid bridge of high Prandtl number fluid, Mech. Eng. Lett. **5**, 1900014 (2019).
[27] H. C. Kuhlmann and E. Hofmann, The mechanics of particle accumulation structures in thermocapillary flows, Eur. Phys. J. Spec. Top. **192**, 3 (2011).
[28] F. Romanò, H. C. Kuhlmann, M. Ishimura, and I. Ueno, Limit cycles for the motion of finite-size particles in axisymmetric thermocapillary flows in liquid bridges, Phys. Fluids **29**, 093303 (2017).
[29] Y. Abe, I. Ueno, and H. Kawamura, Dynamic particle accumulation structure due to thermocapillary effect in noncylindrical half-zone liquid bridge, Ann. N.Y. Acad. Sci. **1161**, 240 (2009).
[30] Y. Niigaki and I. Ueno, Formation of particle accumulation structure (PAS) in half-zone liquid bridge under an effect of thermo-fluid flow of ambient gas, Trans. Jpn. Soc. Aeronaut. Space Sci. **10**, Ph33 (2012).
[31] K. Yamaguchi, T. Hori, and I. Ueno, Long-term behaviors of a single particle forming a coherent structure in thermocapillary-driven convection in half-zone liquid bridge of high Prandtl-number fluid, Int. J. Microgravity Sci. Appl. **36**, 360203 (2019).
[32] A. Toyama, M. Gotoda, T. Kaneko, and I. Ueno, Existence conditions and formation process of second type of spiral loop particle accumulation structure (SL-2 PAS) in half-zone liquid bridge, Microgravity Sci. Technol. **29**, 263 (2017).
[33] Shin-Etsu Chemical Company Limited, Technical Data: Silicone Fluid KF96 Performance Test Results, Tech. Rep., Shin-Etsu Chemical Co., Ltd., 2014, https://www.shinetsusilicone-global.com/catalog/pdf/kf96_e.pdf.
[34] Shin-Etsu Chemical Company Limited, Technical Note: Silicone Oil KF96 (in Japanese), Tech. Rep., Shin-Etsu Chemical Co., Ltd., 2011.
[35] M. Gotoda, T. Sano, T. Kaneko, and I. Ueno, Evaluation of existence region and formation time of particle accumulation structure (PAS) in half-zone liquid bridge, Eur. Phys. J. Spec. Top. **224**, 299 (2015).
[36] K. Nishino, N. Kasagi, and M. Hirata, Three-dimensional particle tracking velocimetry based on automated digital image processing, J. Fluids Eng. **111**, 384 (1989).
[37] F. Romanò and H. C. Kuhlmann (private communication).
[38] H. C. Kuhlmann and F. H. Muldoon, On the different manifestations of particle accumulation structures (PAS) in thermocapillary flows, Eur. Phys. J. Spec. Top. **219**, 59 (2013).